ACS APPLIED ENGINEERING MATERIALS

pubs.acs.org/acsaenm Article

Quantification of Electrode Pulverization Enabled through Operando Video Microscopy of an Electrodeposited Antimony Anode

Rhys A. Otten, Kelly Nieto, Maxwell C. Schulze, and Amy L. Prieto*

Cite This: ACS Appl. Eng. Mater. 2023, 1, 3062−3068 Read Online

ACCESS | Metrics & More | Article Recommendations | Supporting Information

ABSTRACT: Alloying anodes, such as metallic antimony, demonstrate promise as alternative electrode materials for lithium-ion battery systems due to their high theoretical capacity of 660 mA h g^{-1}. However, antimony undergoes anisotropic volume expansion and multiple crystallographic phase transformations upon lithiation and delithiation, which often lead to fracturing or pulverization of the electrode. This pulverization can result in the loss of electrical contact and poor cycling stability. To better understand the degradation mechanism of these electrodes, we demonstrate the use of operando video optical microscopy in tandem with electrochemical testing and a program for the quantification of pulverization for the development of failure mechanism hypotheses. This method is broadly applicable to the characterization and understanding of electrochemically induced mechanical failure mechanisms in high energy density electrodes.

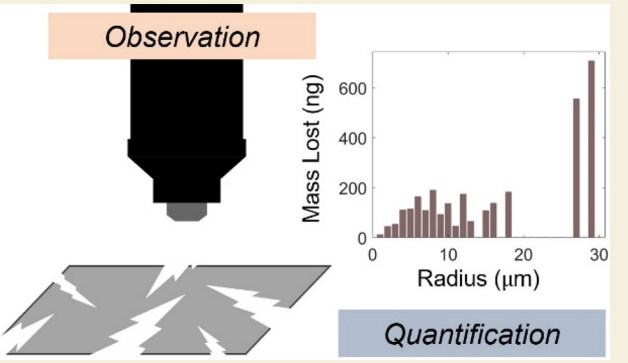

KEYWORDS: *operando video microscopy, lithium ion, battery, electrodeposited anode, alloying, electrode pulverization, volume expansion*

INTRODUCTION

Consumer demand for electronics for every facet of life has increased. At present, lithium-ion (Li-ion) batteries dominate a saturating market for small portable electronics such as smartphones, laptops, power tools, and personal care devices. However, there is an increasing need for higher energy density, longer battery life, and increased safety compared to those that traditional Li-ion batteries offer. Commercial Li-ion batteries often employ a graphite negative electrode (anode) where Li ions are intercalated and deintercalated into, and out of, graphite through a Li-salt-containing, carbonate-based electrolyte, during charge and discharge.[1] One way to increase the energy density of a cell would be to employ alloying anodes, wherein the anodes react directly with Li to produce a daughter compound that gives rise to much higher theoretical capacities.[2−5] Antimony (Sb) is a promising alloy-type anode with a high theoretical capacity, 660 $mAhg^{-1}$, and accessible working potential.[6−8] Alloying reactions, though capable of higher capacities, are subject to coherency strains due to two-phase coexistence,[9] plastic deformation,[10] and volume expansion,[11−14] ultimately leading to fracture and loss of electrical contact.

Failure in antimony electrodes can be linked to volumetric expansion caused by their multiple crystallographic phase transformations observed during alloying with lithium. Antimony is predicted to undergo two phase changes during lithiation, as seen in Figure 1. Lithium insertion into Sb first

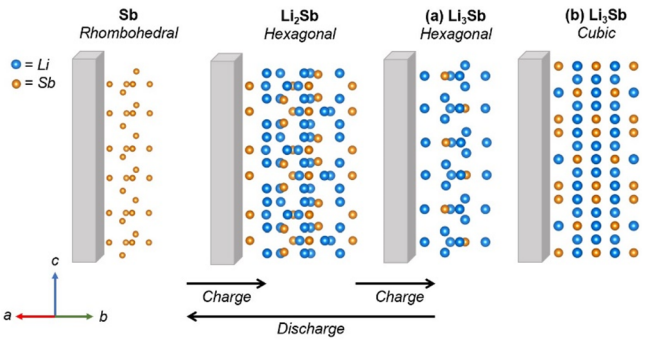

Figure 1. Antimony is theoretically predicted to undergo two phase changes during lithiation (charging). Upon the initial lithiation of Sb, an intermediate Li_2Sb is formed belonging to the hexagonal lattice system. It is then followed by the formation of Li_3Sb, which has been experimentally observed to belong to (a) the hexagonal lattice system or (b) the cubic lattice system. During the removal of Li from Sb, Li_3Sb transforms directly to Sb, bypassing the Li_2Sb phase.

Received: September 6, 2023
Revised: September 22, 2023
Accepted: September 26, 2023
Published: October 19, 2023

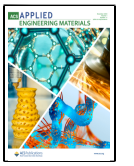

https://doi.org/10.1021/acsaenm.3c00521
ACS Appl. Eng. Mater. 2023, 1, 3062−3068

results in the formation of hexagonal Li_2Sb followed by fully lithiated hexagonal or cubic Li_3Sb.[15] During the removal of Li from Sb, Li_3Sb is predicted to transform directly to Sb, bypassing the intermediate hexagonal Li_2Sb phase.[16] While intercalation compounds such as graphite generally undergo low, isotropic volume expansion, Sb undergoes large volume expansion anisotropically, at 135% relative to the Sb unit cell.[17] The mechanism of this volume expansion and phase transformation as it relates to thermodynamics has been explored, but its contribution to pulverization and mechanical instability is yet uncertain.[18] Early observation of pulverization as a result of electrochemical cycling of an Sb thin film was observed ex situ through electron microscopy.[19] However, ex situ techniques give rise to uncertainty and the potential for mechanical damage due to handling and transport, particularly in the case of samples containing Li, which are highly air-sensitive. In addition, an attempt to quantify the amount of bulk material lost as a result of pulverization has not yet been made.

To better inform our understanding of the mechanisms of mechanical failure in electrode materials, operando monitoring enables the direct observation of mechanical phenomena in batteries during electrochemical cycling. Operando monitoring thus facilitates the coupling of the observation of anode material behavior with electrochemical phenomena in single-particle and bulk materials in real time. Optical operando microscopy has already been used to observe and quantify nucleation, morphology, and particle size effects in lithium systems.[20,21] Additionally, pulverization phenomena, such as cracking in anode materials, have been monitored with operando techniques including optical scattering microscopy and transmission X-ray microscopy, allowing for the proposal of degradation mechanism hypotheses.[22,23] This work combines the efforts of observation through operando video microscopy and quantification through image processing and data analysis of footage obtained therein to inform the degradation insight in novel anode materials. One of the significant advantages of the cell we describe here is the ease of fabrication and use and corresponding low cost.

In this work, we demonstrate both the observation and the quantification of pulverization phenomena in bulk electrodeposited Sb anode films through the calculation of spatial parameters of regions where active material fractured and lost contact with the bulk through the use of a program we developed for analysis. To establish the efficacy of our method, one galvanostatic cycle of an Sb thin film is coupled with plan-view operando video microscopy through the use of an elementary optical cell from which electrochemical data are also extracted. Plan-view video microscopy enables direct observation of bulk anode films as seen from above through the objective of an optical microscope, illuminating the spatial orientation of surface details. Experiments performed in operando couple direct observation with surface changes and their locations arising from lithiation or delithiation of the Sb electrode. Quantifying the size and prevalence of regions of active material loss and their spatial location in an electrode can elucidate the role of mechanical and electrochemical phenomena in the failure of bulk anode films. This allows for a failure mode or mechanism hypothesis to be constructed.

METHODS

Materials for Electrode Fabrication

Lithium cobalt oxide ($LiCoO_2$) electrodes were composed of a slurry of $LiCoO_2$ powder (LCO, Alfa Aesar, 97%), carbon black (Super P, Alfa Aesar, <99%), and poly(vinylidene fluoride) (PVDF, Sigma-Aldrich, Mw ≈ 534 000) at a weight percent ratio of 80:10:10 respectively. The slurry was formulated with 1-methyl-2-pyrrolidinone (NMP, Sigma-Aldrich, ACS reagent, ≥99.0%) as the wetting solvent. Lithium cobalt oxide slurry electrodes were cast onto aluminum foil. The film was then dried in air at 80 °C until visibly dry and then dried in a vacuum oven at 100°C for 1 h.

The Sb electrode was fabricated through electrodeposition. The electrodeposition solution was prepared by mixing 200 mM sodium gluconate (Sigma-Aldrich, ACS reagent) with 30 mM antimony trichloride ($SbCl_3$, Sigma-Aldrich, anhydrous ≥99.0%) in 100 mL of Millipore water. The nickel foil (McMaster Carr, 99.0% Ni, Alloy 200/201, 0.001 in. thickness) current collectors were cleaned and prepared by rinsing with ethanol and then water and by dipping it into a 20% concentrated solution of HNO_3 for 60 s. The electrodeposition solution was titrated to a pH of 6 with a concentrated sodium hydroxide solution. The films were electrodeposited through chronocoulometry onto the cleaned nickel foil at room temperature at −1.05 V vs a saturated calomel electrode with a charge limit of 3 C/cm^2.

Construction of Optical Cell

An elementary optical cell was constructed with distant parallel electrodes enclosed in two parallel glass slides. The counter and reference electrodes (CE, RE) were made from a slurry of LCO on aluminum foil. A 1/8 in. aperture was inserted to allow for plan-view imaging of the working electrode. The working electrode (WE) was an electrodeposited Sb film on Ni foil (Figure S1).

Computational Methods

An ImageJ macro was written wherein we calibrate spatial information for the optical imaging device in terms of pixels by setting a known real distance in micrometers, allowing for simple conversion between micrometers in real space and pixels in each image. Images underwent a simple filter for contrast correction, smoothing, despeckling, and grayscale conversion. Preprocessing steps reduce image noise while limiting potential blurring that is not already present in raw optical data. In Video 1, bulk Sb is gray and darkens with increasing degree of lithiation. Fractured regions where material is lost appear white as the light reflects back to the objective off of the Ni blocking layer below Sb. Infinite circularity approximation is applied by ImageJ when identifying particles (pulverized regions), where a perfect circle is assigned a value of 1. Any imperfect circles have values between 0 and 1. For our purposes, we cannot assume every pulverized region is circular in shape; therefore, all values between 0 and 1 were accepted to be selected by the macro. ImageJ also allows for a threshold of sensitivity to be chosen by the user when selecting particles, but we chose to allow for automatic thresholding to reduce the subjectivity in our analysis.

Computation of quantifiable information such as mass and density of active material loss was aided through the use of superpixels to analyze image data. Superpixels segment an image into larger regions and aid in computing image features by capturing redundancy and improving the speed of computation.[24,25] While many superpixel algorithms exist for image segmentation, we chose to simply bin nearby, like pixels, into rectangular superpixels to reduce processing time while maintaining the relative dimension of the video microscopy footage. The size of the superpixel chosen is related to the resolution in the x-direction and y-direction of the image obtained. In our system, the originally obtained images had a pixel resolution of 1920 × 1440. Generally, fewer superpixels reduce error at the cost of an increase in computation time. We chose to bin 30 × 30 pixels, resulting in a new image with superpixel resolution of 64 × 48. By screening bin sizes through validation tests, this size was

https://doi.org/10.1021/acsaenm.3c00521
ACS Appl. Eng. Mater. 2023, 1, 3062−3068

determined to be the largest that resulted in no data loss and minimal error (Figure S2).

To further reduce error, the first row and column of superpixels that touch the edge of the image are masked, such that partially visible pulverized regions are excluded from the calculation, as they are incomplete and can provide misleading spatial data. Additionally, we assume a more imperfect focus on the edges of our images. An edge cut is performed, wherein the superpixels to be masked are removed. This results in a remaining image area given by eq 1.

$$ImgArea = PhotoArea \times FocusPercent \times \sum_i \frac{\sum_i UnmaskedSuperpixels - MaskBins}{NumMaskBins} \quad (1)$$

A circular two-dimensional area approximation, where the effective radius of a circle corresponding to a particular pulverized region as identified by ImageJ, is used to compute the volume of a sphere is applied.[20] Using the known density of the film being studied, in this case, Sb deposited on Ni, at 6.691 g/cm^3, we extracted the mass that occupied such a region. This calculation assumes both isotropic fracture in three dimensions and a uniform density of the Sb anode film. This approximation is subject to influence from experimental variables, including inhomogeneity in the electrodeposited Sb film and substrate imperfections. However, this analysis allows us to observe quantitative trends within a set of experiments, including a direct comparison of the size, density, and number of fracture regions observed. Effective radius, volume of pulverized region, and mass lost in that region are extracted and stored for each particle. If multiple images are grouped for analysis, for instance if we desire to look at several progressive frames of delithiation data, standard deviation and uncertainty are calculated by the program to check for anomalous counting or extreme pulverization over few frames.

Procedure

Image Processing. Video footage was obtained with an OLYMPUS BXS2 microscope, an OLYMPUS DP22 microscope digital camera, and an UMPlanFI 10x/0.30 BD objective. The collected footage was rendered, enhanced, and scaled to time with Adobe Premiere Pro. Images of individual frames taken from operando video microscopy footage are analyzed using ImageJ processing software. All imaging data were taken relative to the original video footage. Videos were resolved to 1 frame per second (fps), and each frame is extracted for individual analysis as a single image.

Particles are analyzed by iterating through rows and columns of pixels in a given image, finding an edge of a particle, outlining it, and measuring its area in units of squared pixels. Following identification, the spatial coordinate, area, and threshold of all particles identified are each calculated or extracted.

Computational Quantification of Pulverization. Data obtained from ImageJ processing were further analyzed through the use of MATLAB scripts. A MATLAB program for data analysis was developed wherein the user selects a calibrated camera and a microscope combination. It is necessary to know the real distance for a given number of pixels of an image obtained by using a given camera-microscope setup. This enables conversion between dimensions in pixels to distances in microns. Additionally, images should be considered for their relative percentage in focus. Lower than perfect focus images are assigned a decimal value between 0.01 and 0.99, which is subjective to the user.

The program first parses high-resolution images into superpixels. It then counts which superpixels contained fractured material from the ImageJ processing step. Immediately after, the edge cut is applied to remove superpixels that outline the image to avoid including incomplete fracture regions in computation. The remaining image area (eq 1) is used to calculate quantifiables, such as pulverized region area, pulverized region density, and lost mass.

Characterization

The Sb WE was galvanostatically cycled with a Gamry Interface 1010 potentiostat by setting the current rate to C/5 and the voltage range to −1.8 to −3.8 V versus the reduction potential of LCO. The WE potential versus the RE was recorded as a function of time for one cycle, where one point of data was obtained every second. All electrochemical data are processed relative to the original one voltage point per second and then rescaled to fit video footage. No data is lost; cycling time is simply converted to video time, where 1 s of electrochemical data is equal to 0.0169 s of video time (Figure 2E, Video 1).

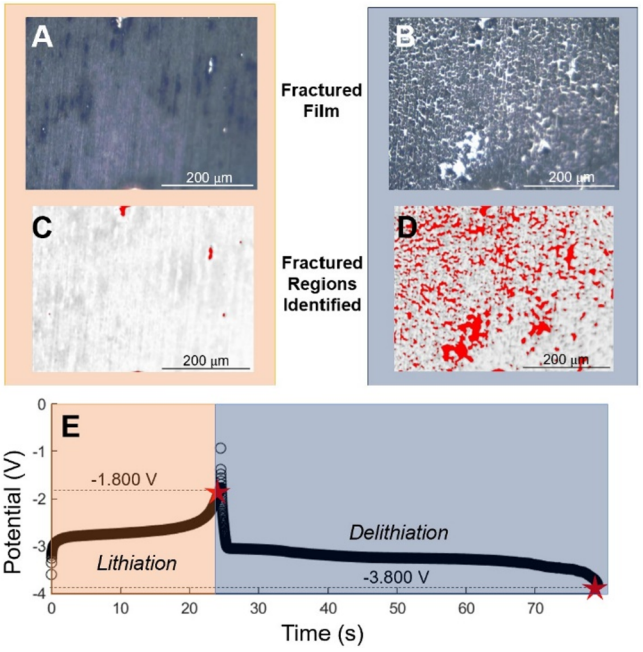

Figure 2. Optical images (A,B) were taken from the operando video footage and show the fully lithiated (A) and the fully delithiated Sb film (B). The pulverized regions were identified through ImageJ for lithiation (C) and delithiation (D). Voltage profile obtained through galvanostatic cycling of Sb in a Li-ion battery with LCO (E). The orange and blue shaded regions correspond to the lithiation and delithiation steps in the cycle, respectively.

The bulk Sb electrode was monitored with operando video microscopy, where each frame of the video collected was extracted and analyzed as a single image. The film was monitored during one galvanostatic cycle to observe changes due to lithiation/delithiation. We first analyzed the total material lost over one cycle, then compared the contribution to total material loss during lithiation versus delithiation, and finally analyzed pulverized region growth during the delithiation step by tracking for each frame obtained.

In addition, differential capacity analysis was used to correlate electrochemical events to changes in the pulverized region growth. Differential capacity plots were generated by cleaning and smoothing cycling data through the method developed by Thompson.[26]

RESULTS AND DISCUSSION

To obtain the total anode material loss over one cycle, the fully delithiated Sb film, which was substantially pulverized, was first analyzed. A map of superpixels that contained pulverized material, 22 × 16 superpixels in dimension, was generated. A colormap was applied to characterize the amount of mass lost in each superpixel, with a brighter color denoting more mass lost (Figure 3A). From this map, it is evident that two superpixels, colored yellow and white by the colormap,

https://doi.org/10.1021/acsaenm.3c00521
ACS Appl. Eng. Mater. 2023, 1, 3062−3068

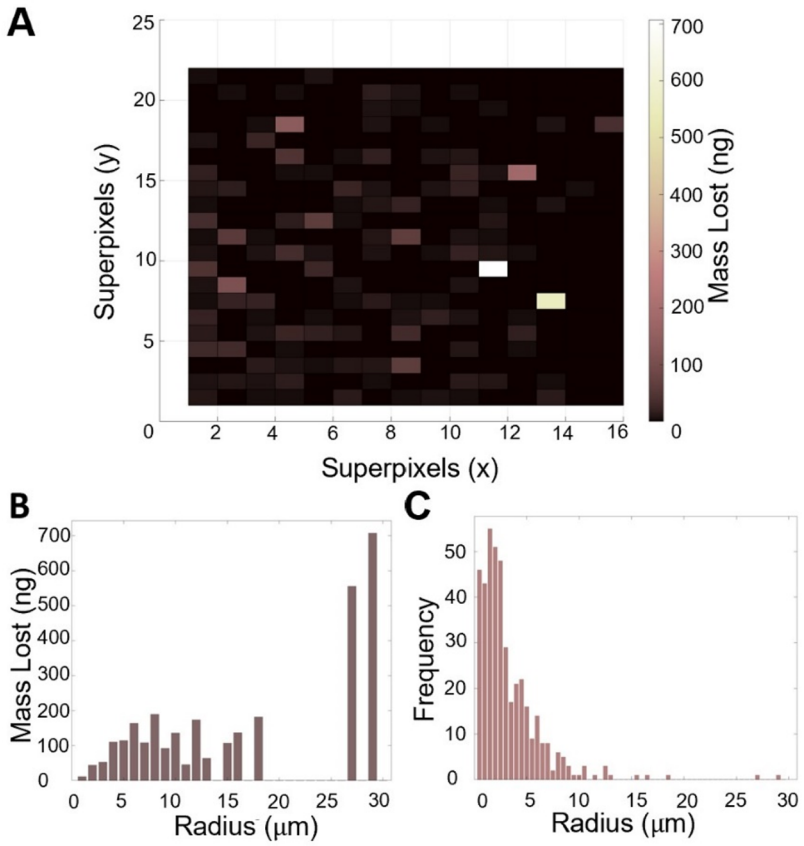

Figure 3. For the fully delithiated, pulverized film: a map of superpixels containing pulverized material, with coordinates in superpixels, wherein mass lost (ng) in each superpixel is correlated to a color intensity, with brighter regions corresponding to more mass lost (A). Mass contribution to total mass loss by radius of pulverized region (B). Number of pulverized regions by size in terms of radius in microns, giving frequency as a function of size (C).

accounted for a substantial loss of anode material in nanograms. Additionally, a plot of the loss of active material in nanograms by total contribution versus radius of pulverized region in units of micrometers is shown (Figure 3B) with a plot of frequency (number) of pulverized regions by size in terms of radius in micrometers (Figure 3C). Each plot demonstrates that the majority of pulverized material in terms of mass is accounted for by two large regions with radii greater than 25 μm, the maximum of which is 29 μm, contributing a total mass loss of 707 ng. However, the majority of pulverized regions are small cracks with radii <10 μm (Figure 3C). These results are also qualitatively observed in Video 1.

From the collected video (Video 1 0:24–1:20), it is apparent that substantial anode material loss occurs during delithiation. The size of the unit cell decreases significantly during the transition from the Li_3Sb phase to the Sb phase (Figure 1). We hypothesize that cracks nucleate during lithiation but are invisible to the observer using a 10× objective. These cracks then grow during delithiation as the film rapidly contracts, inducing substantial pulverization and loss of contact within the film. We quantify this difference by calculating the contribution to total material loss during lithiation and delithiation in terms of total mass and density. For one image obtained after lithiation (Figure 2A, Video 1 0:24) and one image obtained following delithiation (Figure 2B, Video 1 1:20), computing the mass loss after the lithiation step with mass loss after delithiation shows that 97% of total mass lost is due to delithiation processes, with 3240 ng lost. Contribution to density of material lost is also dominated by the delithiation step, with 99% of the total amounting to 218 $\mu g/cm^2$.

Given operando video microscopy footage (Video 1), we can perform analysis on each individual frame obtained, monitoring spatial parameters as they change with optical data as a direct function of electrochemical data. As most optically observable pulverization occurred during delithiation of Sb, it is useful to quantify the change of pulverized region area while Li is removed from the Sb film as a function of the cell voltage. In addition to examining the voltage profile, more information can be gathered when incorporating differential capacity analysis to correlate electrochemical events to pulverization events. In a voltage versus time plot (Figure 4A), electrochemical events appear as plateaus where the capacity changes a large amount for a small change in voltage.[27,28] In Figure 4A, it is evident that significant electrochemical event(s) may be occurring between −3 and −3.25 V. However, if plateaus from different electrochemical events overlap, then it is not possible to deconvolute the contributions of multiple events. Figure 4B shows a differential capacity plot for the discharge (delithiation) step referenced in Figures 2E and 4A with peaks of interest identified (Table 1).

Figure 4C displays the maximum pulverized region area, the average pulverized region area, and the minimum pulverized region area in squared micrometers as a function of cell voltage. The dotted vertical lines in Figure 4C correlate to the

https://doi.org/10.1021/acsaenm.3c00521
ACS Appl. Eng. Mater. 2023, 1, 3062−3068

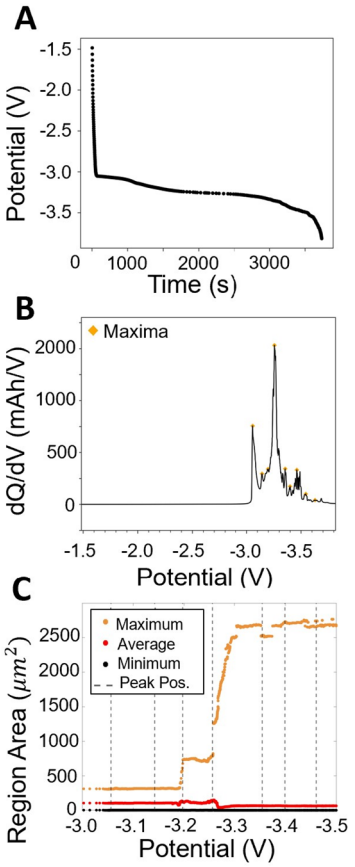

Figure 4. Cell voltage vs test time for delithiation (A). Differential capacity plot for discharge step of the cycle, with data cleaned and smoothed and peaks identified (B). Pulverized region area as a function of increasingly negative cell voltage with peaks from (B) shown as dotted gray lines (C). The orange trace corresponds to the maximum pulverized region area, the red trace is the weighted average pulverized region area, and the black trace is the minimum.

Table 1. Peaks Identified through Differential Capacity Analysis Are Shown in Figure 4B

Peak Number	Voltage
1	−3.06 V
2	−3.14 V
3	−3.20 V
4	−3.26 V
5	−3.35 V
6	−3.40 V
7	−3.46 V
8	−3.54 V
9	−3.63 V

peaks highlighted in the differential capacity analysis in Figure 4B. There are more data points at more negative cell potentials due to the amount of time the cell experienced a voltage lower than −3 V (Figure 4A). It is evident that the maximum pulverized region area grew precipitously after the cell reached this potential. Notable here is the significant increase in maximum pulverized region area at a cell voltage of approximately −3.2 V and further at −3.25 V. These increases directly correlate to the third and fourth peaks in Figure 4B and Table 1, with calculated cell voltages of −3.20 and −3.26 V, respectively. The fourth peak (−3.25 V) in Figure 4B likely results from the removal of a large amount of lithium from the anode or the transformation of Li_3Sb to Sb, which would lead to a significant contraction in the anode and, in turn, to a massive increase in area of the pulverized region (Figure 4C).[29,30] The appearance of several delithiation peaks instead of one distinct delithiation event could be attributed to nonuniform lithiation in the electrodeposited film, leading to stages of delithiation in different regions of the anode. It is noted here that the average pulverized region area also decreases in size past −3.25 V and the fourth peak, which is seemingly contradictory to the trend experienced by the maximum area (Figures S4 and S5). However, from Figure 3, it is known that only two regions of pulverization are significantly large, while there are numerous small cracks tracked by the program. The average calculated here is weighted by frequency, so the appearance of many small cracks would, in turn, drive down the average, while the existence of only two large regions (Figure 3B) is not sufficient to drive up the mean. The appearance of these small cracks is also supported by the video (Video 1 0:51−1:20).

CONCLUSION

We have demonstrated the ability to quantify pulverization phenomena in terms of physical material lost of an electrodeposited, thin film, Sb negative electrode. The demonstrated results emphasize the utility of operando optical microscopy in facilitating coupled electrochemical experiments with the observation of mechanical degradation in the electrode material. Observation of the behavior of a Sb anode during galvanostatic cycling reveals that observable pulverization occurs primarily during delithiation.

Observable pulverization does not suggest that pulverization occurs only during delithiation, however. Knowledge of the significant volume expansion upon lithiation undergone by Sb leads to the hypothesis that pulverization initiates, or cracks nucleate, during this step of cycling, but contraction of the film upon delithiation leads to crack growth and more visible detection. We have shown that delithiation causes significant crack growth and also multiplication in the form of many smaller cracks emerging. We have also quantified the material loss due to pulverization events in terms of the mass and density for our system.

This system facilitates operando observation of electrode behavior in response to other parameters known to affect electrode performance, such as electrolyte selection, composition, crystallinity, and fabrication technique. This method provides a tool to quantify the effects of changes in these parameters. The electrochemical experiment is also not limited to galvanostatic cycling. Battery degradation and electrode behavior can be observed and coupled with variable charge and discharge rates, constant voltage experiments, and constant current with constant voltage to investigate electrochemical and mechanical responses. The observation of macroscopic mechanical changes in response to the alteration of electrochemical parameters is thus enabled.

Additionally, the results demonstrate that this method can be used to quantify and observe pulverization in alloy-type electrodes broadly. Operando visualization, enabled using an optical microscopy cell that is nonspecific to the material of choice, allows for the study of any film of interest. Quantification is accomplished through computational methods that require only images obtained through optical microscopy and a relation between image space and real space.

https://doi.org/10.1021/acsaenm.3c00521
ACS Appl. Eng. Mater. 2023, 1, 3062−3068

■ ASSOCIATED CONTENT

Supporting Information

The Supporting Information is available free of charge at https://pubs.acs.org/doi/10.1021/acsaenm.3c00521.

Optical cell (Figure S1), segmentation tests (Figure S2), pulverized region area versus cell voltage (Figures S3–S7) (PDF)

Video 1: Synchronized operando video footage of Sb working electrode for one galvanostatic cycle and voltage profile (ZIP)

■ AUTHOR INFORMATION

Corresponding Author

Amy L. Prieto − *Department of Chemistry, Colorado State University, Fort Collins, Colorado 80523, United States;* orcid.org/0000-0001-9235-185X; Email: amy.prieto@colostate.edu

Authors

Rhys A. Otten − *School of Advanced Materials Discovery, Colorado State University, Fort Collins, Colorado 80523, United States;* orcid.org/0000-0001-7180-7037

Kelly Nieto − *Department of Chemistry, Colorado State University, Fort Collins, Colorado 80523, United States;* orcid.org/0000-0002-8833-0113

Maxwell C. Schulze − *Department of Chemistry, Colorado State University, Fort Collins, Colorado 80523, United States*

Complete contact information is available at: https://pubs.acs.org/10.1021/acsaenm.3c00521

Notes

The authors declare no competing financial interest.

■ ACKNOWLEDGMENTS

The authors wish to thank the Sambur Group at Colorado State University for the OLYMPUS DP22 microscope digital camera and debugging assistance. Additionally, we wish to thank Chris Hjelmfelt for her willingness to share her expertise in data analysis, as well as the rest of the Schnee Group at South Dakota School of Mines, whose prior work has inspired parts of this methodology. This work was partially funded by NSF SSMC- 2211067. K.N. was supported in part through an American Dissertation Fellowship from the American Association of University Women (AAUW).

■ REFERENCES

(1) Xie, J.; Lu, Y. C. A retrospective on lithium-ion batteries. *Nat. Commun.* **2020**, *11*, 2499.

(2) Park, C. M.; Kim, J. H.; Kim, H.; Sohn, H. J. Li-alloy based anode materials for Li secondary batteries. *Chem. Soc. Rev.* **2010**, *39*, 3115−3141.

(3) Thackeray, M. M.; Vaughey, J. T.; Johnson, C. S.; Kropf, A. J.; Benedek, R.; Fransson, L. M. L.; Edstrom, K. Structural Considerations of Intermetallic Electrodes for Lithium Batteries. *J. Power Sources* **2003**, *113* (1), 124−130.

(4) Cabana, J.; Monconduit, L.; Larcher, D.; Palacín, M. R. Beyond Intercalation-Based Li-Ion Batteries: The State of the Art and Challenges of Electrode Materials Reacting through Conversion Reactions. *Adv. Mater.* **2010**, *22* (35), E170.

(5) Obrovac, M. N.; Chevrier, V. L. Alloy Negative Electrodes for Li-Ion Batteries. *Chem. Rev.* **2014**, *114* (23), 11444−11502.

(6) Sun, Q.; Li, W.-J.; Fu, Z.-W. A Novel Anode Material of Antimony Nitride for Rechargeable Lithium Batteries. *Solid State Sci.* **2010**, *12* (3), 397−403.

(7) Tian, W.; Zhang, S.; Huo, C.; Zhu, D.; Li, Q.; Wang, L.; Ren, X.; Xie, L.; Guo, S.; Chu, P. K.; Zeng, H.; Huo, K. Few-Layer Antimonene: Anisotropic Expansion and Reversible Crystalline-Phase Evolution Enable Large-Capacity and Long-Life Na-Ion Batteries. *ACS Nano* **2018**, *12* (2), 1887−1893.

(8) He, J.; Wei, Y.; Zhai, T.; Li, H. Antimony-Based Materials as Promising Anodes for Rechargeable Lithium-Ion and Sodium-Ion Batteries. *Materials Chemistry Frontiers* **2018**, *2* (3), 437−455.

(9) Van der Ven, A.; Garikipati, K.; Kim, S.; Wagemaker, M. The Role of Coherency Strains on Phase Stability in Li_xPO_4: Needle Crystallites Minimize Coherency Strain and Overpotential. *Journal of The Electrochemical Society* **2009**, *156* (11), A949.

(10) Mukhopadhyay, A.; Sheldon, B. W. Deformation and Stress in Electrode Materials for Li-Ion Batteries. *Prog. Mater. Sci.* **2014**, *63*, 58−116.

(11) Tarascon, J.-M.; Armand, M. Issues and Challenges Facing Rechargeable Lithium Batteries. *Nature* **2001**, *414* (6861), 359−367.

(12) Sung, J.; Kim, N.; Kim, S.-P.; Lee, T.; Yoon, M.; Cho, J. Highly Densified Fracture-Free Silicon-Based Electrode for High Energy Lithium-Ion Batteries. *Batteries & Supercaps* **2022**, *5* (9), No. e202200136.

(13) Choi, S.-H.; Nam, G.; Chae, S.; Kim, D.; Kim, N.; Kim, W. S.; Ma, J.; Sung, J.; Han, S. M.; Ko, M.; Lee, H.-W.; Cho, J. Robust Pitch on Silicon Nanolayer−Embedded Graphite for Suppressing Undesirable Volume Expansion. *Adv. Energy Mater.* **2019**, *9* (4), No. 1803121.

(14) Ma, J.; Sung, J.; Lee, Y.; Son, Y.; Chae, S.; Kim, N.; Choi, S.-H.; Cho, J. Strategic Pore Architecture for Accommodating Volume Change from High Si Content in Lithium-Ion Battery Anodes. *Adv. Energy Mater.* **2020**, *10* (6), No. 1903400.

(15) Park, C.-M.; Yoon, S.; Lee, S.-I.; Kim, J.-H.; Jung, J.-H.; Sohn, H.-J. High-Rate Capability and Enhanced Cyclability of Antimony-Based Composites for Lithium Rechargeable Batteries. *J. Electrochem. Soc.* **2007**, *154* (10), A917.

(16) Hewitt, K. C.; Beaulieu, L. Y.; Dahn, J. R. Electrochemistry of Insb as a Li Insertion Host: Problems and Prospects. *J. Electrochem. Soc.* **2001**, *148* (5), A402.

(17) Mayo, M.; Morris, A. J. Structure Prediction of Li−Sn and Li−Sb Intermetallics for Lithium-Ion Batteries Anodes. *Chem. Mater.* **2017**, *29* (14), 5787−5795.

(18) Chang, D.; Huo, H.; Johnston, K. E.; Ménétrier, M.; Monconduit, L.; Grey, C. P.; Van der Ven, A. Elucidating the Origins of Phase Transformation Hysteresis during Electrochemical Cycling of Li-Sb Electrodes. *Journal of Materials Chemistry A* **2015**, *3* (37), 18928.

(19) Jackson, E. D.; Mosby, J. M.; Prieto, A. L. Evaluation of the Electrochemical Properties of Crystalline Copper Antimonide Thin Film Anodes for Lithium Ion Batteries Produced by Single Step Electrodeposition. *Electrochim. Acta* **2016**, *214*, 253−264.

(20) Sanchez, A. J.; Kazyak, E.; Chen, Y.; Chen, K. H.; Pattison, E. R.; Dasgupta, N. P. Plan-View Operando Video Microscopy of Li Metal Anodes: Identifying the Coupled Relationships among Nucleation, Morphology, and Reversibility. *ACS Energy Letters* **2020**, *5* (3), 994−1004.

(21) Sandoval, S. E.; Cortes, F. J. Q.; Klein, E. J.; Lewis, J. A.; Shetty, P. P.; Yeh, D.; McDowell, M. T. Understanding the Effects of Alloy Films on the Electrochemical Behavior of Lithium Metal Anodes with Operando Optical Microscopy. *J. Electrochem. Soc.* **2021**, *168* (10), No. 100517.

(22) Merryweather, A. J.; Jacquet, Q.; Emge, S. P.; Schnedermann, C.; Rao, A.; Grey, C. P. Operando monitoring of single-particle kinetic state-of-charge heterogeneities and cracking in high-rate Li-ion anodes. *Nat. Mater.* **2022**, *21*, 1306.

(23) Selvaraj, B.; Wang, C. C.; Song, Y. F.; Sheu, H. S.; Liao, Y. F.; Wu, N. L. Remarkable microstructural reversibility of antimony in sodium ion battery anodes. *Journal of Materials Chemistry A* **2020**, *8* (43), 22620−22625.

(24) Stutz, D.; Hermans, A.; Leibe, B. Superpixels: An Evaluation of the State-of-the-Art. *Computer Vision and Image Understanding* **2018**, *166*, 1−27.
(25) Wang; Liu, X.; Gao, Y.; Ma, X.; Soomro, N. Q. Superpixel segmentation: A benchmark. *Signal Processing. Image Communication* **2017**, *56*, 28−39.
(26) Thompson, N. L. Total Differential Capacity Plot Analysis Using Data Science Methods. M.S. Thesis, University of Washington, 2018.
(27) Olson, J. Z.; López, C. M.; Dickinson, E. J. F. Differential Analysis of Galvanostatic Cycle Data from Li-Ion Batteries: Interpretative Insights and Graphical Heuristics. *Chem. Mater.* **2023**, *35* (4), 1487−1513.
(28) Marzocca, L. M.; Atwater, T. B. *Differential Capacity-Based Modeling for In-Use Battery Diagnostics, Prognostics, and Quality Assurance*; AD1018791; Defense Technical Information Center, 2014.
(29) Wang, N.; Bai, Z.; Qian, Y.; Yang, J. Double-Walled Sb@TiO2-x Nanotubes as a Superior High-Rate and Ultralong-Lifespan Anode Material for Na-Ion and Li-Ion Batteries. *Adv. Mater.* **2016**, *28* (21), 4126−4133.
(30) Schulze, M. C.; Schulze, R. K.; Prieto, A. L. Electrodeposited Thin-Film CuxSb Anodes for Li-Ion Batteries: Enhancement of Cycle Life via Tuning of Film Composition and Engineering of the Film-Substrate Interface. *J. Mater. Chem. A* **2018**, *6* (26), 12708−12717.

https://doi.org/10.1021/acsaenm.3c00521
ACS Appl. Eng. Mater. 2023, 1, 3062−3068